Research Square

Preprints are preliminary reports that have not undergone peer review.
They should not be considered conclusive, used to inform clinical practice,
or referenced by the media as validated information.

Numerical modelling of seismic-wave interaction with a magmatic plumbing system

Deepak Garg

deepak.garg@ingv.it

National Institute of Geophysics and Volcanology

Antonella Longo

National Institute of Geophysics and Volcanology

Paolo Papale

National Institute of Geophysics and Volcanology

Research Article

Keywords: Magma plumbing systems, Earthquake-volcano interactions, Seismic shaking, Magma mixing, Overpressure evolution

Posted Date: June 17th, 2026

DOI: https://doi.org/10.21203/rs.3.rs-9930966/v1

License: This work is licensed under a Creative Commons Attribution 4.0 International License.
Read Full License

Additional Declarations: No competing interests reported.

Numerical modelling of seismic-wave interaction with a magmatic plumbing system

Deepak Garg* Antonella Longo Paolo Papale

Istituto Nazionale di Geofisica e Vulcanologia (INGV), Pisa, Italy
Antonella Longo ORCID: 0000-0001-6590-6346
Paolo Papale ORCID: 0000-0002-5207-2124

Abstract

Strong earthquakes may influence the dynamics of magmatic systems and potentially affect their evolution toward eruptive conditions. Understanding the physical response of magma reservoirs to seismic shaking is therefore important for assessing volcano behaviour following large earthquakes. In this work, we present a numerical model that computes the space-time evolution of magma properties while accounting for deformation of the domain boundaries induced by seismic waves. Numerical simulations are performed for a magmatic plumbing system composed of shallow and deep magma chambers connected by a dike. Two representative magma compositions are considered, reproducing typical volcanic settings in which a more evolved and partially degassed magma occupies the shallow reservoir. The results show that seismic shaking generates transient overpressure oscillations of several MPa throughout the system. These oscillations are spatially non-uniform and are amplified within the dike, while the overall mixing dynamics and flow velocities remain largely unaffected. The response is stronger for lower-viscosity magmas, which transmit pressure disturbances more efficiently. Although the pressure oscillations decay after the passage of the seismic wave, the resulting overpressure remains significantly higher than in equivalent simulations without shaking. In some cases, peak overpressure oscillations reach approximately 5 MPa within the dike. These results indicate that seismic shaking can substantially modify the pressure state of a magmatic system even when its large-scale flow dynamics remain largely unchanged.

Keywords: Magma plumbing systems; Earthquake-volcano interactions; Seismic shaking; Magma mixing; Overpressure evolution

*Corresponding author: deepak.garg@ingv.it
ORCID: 0000-0003-2463-5185

1 Introduction

Earthquakes and volcanic eruptions commonly occur in tectonically active regions, particularly along convergent plate boundaries. Their interaction is bidirectional: magma migration can alter the stress state of surrounding faults and potentially trigger earthquakes (Thatcher and Savage, 1982), whereas earthquakes can perturb magma plumbing systems and influence volcanic activity (Nishimura, 2017). Previous studies suggest that an earthquake can affect a magma body by changing the stress of the surrounding rocks (Marzocchi, 2002; Fujita et al., 2013). The internal response of a magma body may include bubble nucleation (Crews and Cooper, 2014), rectified diffusion (Ichihara and Brodsky, 2006), and advective overpressure (Manga and Brodsky, 2006). Many studies have proposed correlations between large earthquakes and increased volcanic activity (Linde and Sacks, 1998; Hill et al., 2002; Alam and Kimura, 2004; Manga and Brodsky, 2006; Manga et al., 2009; Eggert and Walter, 2009; Toda et al., 2011). The phenomenon has been examined in case studies (Walter and Amelung, 2006; Lara et al., 2004) and by statistical analysis (Marzocchi et al., 2002; Bebbington and Marzocchi, 2011; Linde et al., 1994; Watt et al., 2009). Earthquakes may precede a large-scale change in magma dynamics and in some cases even eruptions (Thatcher and Savage, 1982; Marzocchi et al., 2002; Jachens and Eaton, 1980). Statistical studies suggest that earthquake-triggered eruptions are relatively rare, representing only a small fraction of global volcanic eruptions (Manga and Brodsky, 2006; Bebbington and Marzocchi, 2011).

Several observations suggest a causal link between large earthquakes and volcanic activity. The 1960 Mw 9.5 Valdivia earthquake in Chile was followed two days later by the eruption of Puyehue-Cordón Caulle volcano (Linde and Sacks, 1998; Eggert and Walter, 2009; Lara et al., 2004), while the 1975 Mw 7.2 Kalapana earthquake was immediately followed by a short-lived eruption at Kīlauea (Jachens and Eaton, 1980). Increased volcanic unrest was also reported throughout Japan after the 2011 Mw 9.0 Tohoku-Oki earthquake (Fujita et al., 2013; Takada and Fukushima, 2013), and the 1992 Landers earthquake triggered activity at volcanic and geothermal systems up to 1200 km from the epicentral region (Hill et al., 2002). Conversely, other large earthquakes, including the 2010 Mw 8.8 Maule earthquake and the 2004 Mw 9.3 Sumatra earthquake, were not followed by widespread eruptive activity (Lay et al., 2010; Pritchard et al., 2013; Manga and Brodsky, 2006). Similarly, in 1996 an intense swarm of volcano-tectonic earthquakes (max Mw 5.1) beneath Akutan Island in the Aleutian volcanic arc, Alaska, produced extensive ground cracks but no eruption of Akutan volcano (Zong et al., 2000). These contrasting observations indicate that the mechanisms controlling earthquake-volcano interactions remain incompletely understood

Although there is substantial evidence that the two phenomena can interact with each other, the impact of an earthquake on magma dynamics has not been understood completely. Existing literature suggests several mechanisms

through which earthquakes may trigger eruptions, however, these mechanisms remain poorly constrained. Very little research has been carried out on the physical effects of seismic waves interacting with magma systems (Walter and Amelung, 2007; Manga and Brodsky, 2006; Namiki et al., 2016). Namiki et al. (2016) investigated the problem in the laboratory by sloshing liquid columns with a foam layer on the top. Previous numerical studies have mainly focused on stress changes induced by earthquakes in the host rocks surrounding magma reservoirs (Walter and Amelung, 2007; Bonali et al., 2012). In such approaches, the computed stress perturbation is used to infer the possible response of the magmatic system without explicitly modelling magma dynamics. More recent studies have investigated the interaction between seismic waves and volcanic conduits (Jousset et al., 2004; Sturton and Neuberg, 2003; Óscar E. Cadena and Sánchez, 2022) or magma chambers through elastodynamic simulations (Limberger and Rümpker, 2024). While these models provide valuable information on stress propagation and wave reverberation, they do not directly resolve the evolution of magma properties such as pressure, composition, gas content, and flow velocity during the passage of a seismic wave through the magmatic system. Consequently, the physical response of a magmatic system to seismic shaking remains poorly constrained. In particular, the evolution of magma overpressure during and after the passage of seismic waves remains largely unexplored.

The existing literature suggests that strong earthquakes may perturb volcanic systems, although the mechanisms by which seismic waves influence magma dynamics remain poorly understood. It is therefore conceivable that an actively evolving magmatic system may respond to seismic shaking through changes in its internal pressure state, potentially modifying its eruptive potential. In this work, we investigate this hypothesis through numerical simulations of a gravitationally unstable magmatic plumbing system composed of shallow and deep reservoirs connected by a dike. Numerical simulations of compressible multiphase magma flow in deforming domains induced by seismic waves are performed through our open-source multiphysics finite element code, GALES (Longo et al., 2012; Garg, 2017; Garg et al., 2021). Simulations with and without seismic forcing are compared in order to quantify the influence of seismic shaking on magma dynamics. The results show that, although the overall mixing dynamics and flow velocities are only weakly affected, seismic shaking generates significant overpressure fluctuations that may locally reach values comparable to or greater than the tensile strength of the surrounding rocks.

2 Numerical model

The magmatic system is modelled as a homogeneous multiphase–multicomponent mixture governed by the compressible conservation equations of mass and momentum together with transport equations for chemical components. Seismic shaking induces deformation of the magmatic domain boundaries, which is accounted for through a moving-mesh formulation. The governing equa-

tions are solved using a stabilized space–time finite element method implemented in the open-source multiphysics code, GALES (Longo et al., 2012; Garg et al., 2018a; Longo et al., 2023, and the GALES repository at `https://gitlab.com/dgmaths9/gales`). The numerical framework allows the simultaneous treatment of compressible magma flow, volatile exsolution, and deforming computational domains.

2.1 Magma flow model

We use a two-dimensional multicomponent flow model to simulate magma dynamics (Longo et al., 2012; Garg et al., 2018a; Longo et al., 2023). The model computes viscous laminar flow of a homogeneous magmatic mixture in both compressible and incompressible regimes. Volatile species are allowed to partition between dissolved and exsolved phases according to local pressure, temperature, and composition (PTX) conditions. The model solves conservation of mass for the mixture, conservation of momentum for the mixture, and conservation of mass for $n-1$ independent components. Temperature is prescribed and therefore an energy conservation equation is not solved. The governing equations are written in the Arbitrary Lagrangian Eulerian (ALE) form using the space-time Piola transformation

$$\boldsymbol{U}_{,t}|_{\hat{x}} + \boldsymbol{F}^a_{i,i} - \hat{v}_i \boldsymbol{U}_{,i} - \boldsymbol{F}^d_{i,i} - \boldsymbol{S} = 0 \tag{1}$$

with

$$\boldsymbol{U} = \begin{bmatrix} \rho \\ \rho v_1 \\ \rho v_2 \\ \rho Y_k \end{bmatrix} \qquad \boldsymbol{F}^a_i = \begin{bmatrix} \rho v_i \\ \rho v_i v_1 \\ \rho v_i v_2 \\ \rho v_i Y_k \end{bmatrix} \qquad \boldsymbol{F}^d_i = \begin{bmatrix} 0 \\ \sigma_{1i} \\ \sigma_{2i} \\ -J_{ki} \end{bmatrix} \qquad \boldsymbol{S} = \begin{bmatrix} 0 \\ \rho g_1 \\ \rho g_2 \\ 0 \end{bmatrix}$$

where $\boldsymbol{U}$ is the conservation variables vector, $\boldsymbol{F}^a_{i,i}$ is the advective flux vector, $\boldsymbol{F}^d_{i,i}$ is the diffusive flux vector, $\boldsymbol{S}$ is the source vector. $()_{,t}|_{\hat{x}}$ denotes a partial time derivative holding the referential coordinates $\hat{x}$ fixed. $\hat{v}_i$ is the ith component of the domain velocity $\hat{\boldsymbol{v}}$. ρ is the mixture density, v_i is the ith component of the mixture velocity $\boldsymbol{v}$, g_i is the ith component of gravitational acceleration. Y_k is kth component of mass fraction vector $\boldsymbol{Y} = \{Y_1, Y_2, \ldots, Y_n\}$ satisfying $\sum_{k=1}^{n} Y = 1$.

The stress tensor components are modeled as

$$\sigma_{ij} = \mu(v_{i,j} + v_{j,i}) - (p - \frac{2}{3}\,\mu\, v_{k,k})\delta_{ij}$$

where p is pressure, μ is the mixture viscosity, δ is kronecker delta. The mass diffusion flux J_{ki} is modeled with Fick's law

$$J_{ki} = -\rho D_k Y_{k,i} \qquad \sum_{k=1}^{n} J_{ki} = 0$$

where D_k is the mass diffusion coefficient.

The conservation equations are closed by an equation of state linking density to local pressure, temperature, and composition. We use a combination of different models to compute the space-time distribution of magma properties. The density of the silicate melt is computed using the model of Lange (1994). For dissolved volatile species we adopt the formulation of Burnham et al. (1969), whereas the gas phase is treated as an ideal gas. The mixture density is computed according to $\rho^{-1} = \sum_i y_i/\rho_i$, where ρ_i is the density of the ith component.

The partitioning of H_2O and CO_2 between dissolved and exsolved phases is computed using the non-ideal multicomponent saturation model of Papale et al. (2006), which accounts for thermodynamic equilibrium between liquid and gas phases. This model provides the spatial and temporal distribution of volatile content required for evaluating magma compressibility and the propagation of pressure disturbances through the magmatic system.

Maximum gas volume fractions in the simulations remain below 4 vol%, corresponding to sub-millimetre bubbles. Under these conditions the homogeneous-mixture assumption remains valid and the rheology can be treated as Newtonian (Giordano et al., 2008; Ishii and Zuber, 1979). The viscosity of the individual magma components is computed following the formulation described in (Giordano et al., 2008; Ishii and Zuber, 1979). The viscosity of the mixture is modelled as $\mu = \sum_i x_i \mu_i$, where x_i and μ_i are the mole fraction and the viscosity of the ith mixture component.

The governing equations are solved for the variable set $p, v_1, v_2, Y_1, \ldots, Y_{n-1}$ using a SUPG stabilized finite element method (Longo et al., 2012; Garg et al., 2018b; Garg and Papale, 2022). The formulation employs residual-based stabilization terms that allow robust computations in advection-dominated and compressible-to-incompressible flow regimes. The numerical implementation supports distributed-memory parallel execution and has been extensively validated against standard benchmark problems.

2.2 Mesh motion model

To account for seismic shaking, the governing equations are solved on a deforming computational domain. An arbitrary Lagrangian–Eulerian (ALE) description is adopted, allowing the mesh to move independently from the fluid while accurately tracking moving boundaries and interfaces. The ALE finite element

formulation naturally incorporates the evolving geometry and the associated mesh motion.

The displacement of boundary nodes is prescribed according to the imposed seismic forcing, whereas the displacement of interior mesh nodes is computed using the elastic deformation method (Tezduyar, 2003; Garg, 2017). In this approach the computational mesh is treated as a fictitious elastic solid and its deformation is obtained by solving the linear elastostatic equations

$$\nabla \cdot \Big(\mu_m(\boldsymbol{\nabla u} + \boldsymbol{\nabla u}^T) + \lambda_m(\boldsymbol{\nabla \cdot u})\boldsymbol{I}\Big) = 0 \tag{2}$$

where λ_m and μ_m are lamé coefficients and $\boldsymbol{u} = \{u_1, u_2\}^T$ is the deformation vector.

In order to tackle the issue of extreme element deformations, the Jacobian based stiffening procedure is adopted. This procedure stiffens smaller elements relative to larger ones, thereby distributing the deformation more uniformly throughout the mesh. This procedure is applied at the level of the finite element integration of Eq. 2 and reads:

$$\int_\Omega [\ldots]\, d\Omega = \sum_e \int_\varepsilon [\ldots]^e\, J^e d\varepsilon \rightarrow \sum_e \int_\varepsilon [\ldots]^e\, J^e \left(\frac{J^0}{J^e}\right)^\chi d\varepsilon \tag{3}$$

where, ε is the finite element reference domain, $[\ldots]$ represents the quantity to be integrated, J^e is the Jacobian for the element e, χ is the degree by which the smaller elements are rendered stiffer than the larger ones, and J^0 is an arbitrary scaling parameter inserted into the formulation to make the alteration dimensionally consistent and is set equal to one. This method stiffens each element by a factor $(J^e)^{-\chi}$. The best values of the stiffening factor have been discussed in Stein et al. (2003), and in this work it is adopted the value of 0.8.

The finite element fluid solution needs the mesh velocity to define the space-time Jacobian of elements evolving from t_n to t_{n+1} (Garg, 2017), therefore, the coordinates of each element are updated to:

$$\boldsymbol{x}_{n+1} = \boldsymbol{x}_n + \boldsymbol{\Delta u} = \boldsymbol{x}_n + \hat{\boldsymbol{v}}\Delta t \tag{4}$$

where $\boldsymbol{x}_{n+1}$ and $\boldsymbol{x}_n$ are the node coordinates at time level t_{n+1} and t_n respectively, $\boldsymbol{\Delta u}$ is the mesh deformation and $\Delta t = t_{n+1} - t_n$.

The overall moving fluid domain is solved by means of a segregated algorithm to solve the fluid flow and the mesh deformation problems separately at each time step. Given the flow domain and flow variables at t_n, the algorithm follows these steps for t_{n+1}

Step 1: Calculate the mesh deformation at the moving boundaries from the fluid velocities at the free boundary and from the earthquake forcing at the Dirichlet boundary.

Table 1: Composition of magmas: Shoshonite (S), Phonolite (P), Andesite (A) and Dacite (D)

	Volatiles		Major oxides									
	H_2O	CO_2	SiO_2	TiO_2	Al_2O_3	Fe_2O_3	FeO	MnO	MgO	CaO	Na_2O	K_2O
S	2	1	52.40	0.85	17.60	1.88	5.74	0.12	3.60	7.93	3.43	4.28
P	1	0.1	53.52	0.60	19.84	1.60	3.20	0.14	1.76	6.76	4.66	7.91
A	4	1	58.70	0.88	17.24	3.31	4.09	0.14	3.37	6.88	3.53	1.64
D	3	0.3	65.98	0.59	16.15	2.47	2.33	0.09	1.81	4.38	3.85	2.20

Step 2: Solve the elasticity equation (2) for the mesh deformation $\boldsymbol{u}$ by specifying the deformation, computed in Step 1, as Dirichlet boundary condition.

Step 3: Compute mesh velocity $\hat{\boldsymbol{v}}$ from the displacement increment.

Step 4: Obtain the new domain via equation (4).

Step 5: Solve Eq. (1) for the flow variables.

Validation of the mesh-deformation algorithm and FEM formulation was performed using several benchmark problems, including the squeezing can, rotating circle, horizontal moving cylinder, broken dam and solitary wave propagation. Detailed descriptions and results are provided in the Electronic Supplementary Material.

3 Numerical simulations

Four numerical simulations are performed to investigate the influence of seismic shaking on magma dynamics. Two simulations consider buoyancy-driven magma convection in the absence of seismic forcing, whereas two additional simulations employ identical initial conditions but include the passage of a strong seismic wave. For each forcing condition, two representative magmatic systems are considered: a shoshonite–phonolite (SP) system, representative of evolved alkaline volcanic provinces such as Vesuvius and Campi Flegrei, and an andesite–dacite (AD) system, representative of typical subduction-zone volcanism. The simulations are defined as follows:

(i) Case 1: shoshonite–phonolite (SP) system without seismic shaking;
(ii) Case 2: andesite–dacite (AD) system without seismic shaking;
(iii) Case 3: shoshonite–phonolite (SP) system with seismic shaking; and
(iv) Case 4: andesite–dacite (AD) system with seismic shaking.

The deep reservoir is represented by an elongated elliptical chamber whose roof lies at approximately 8 km depth and whose base reaches 9 km depth. The

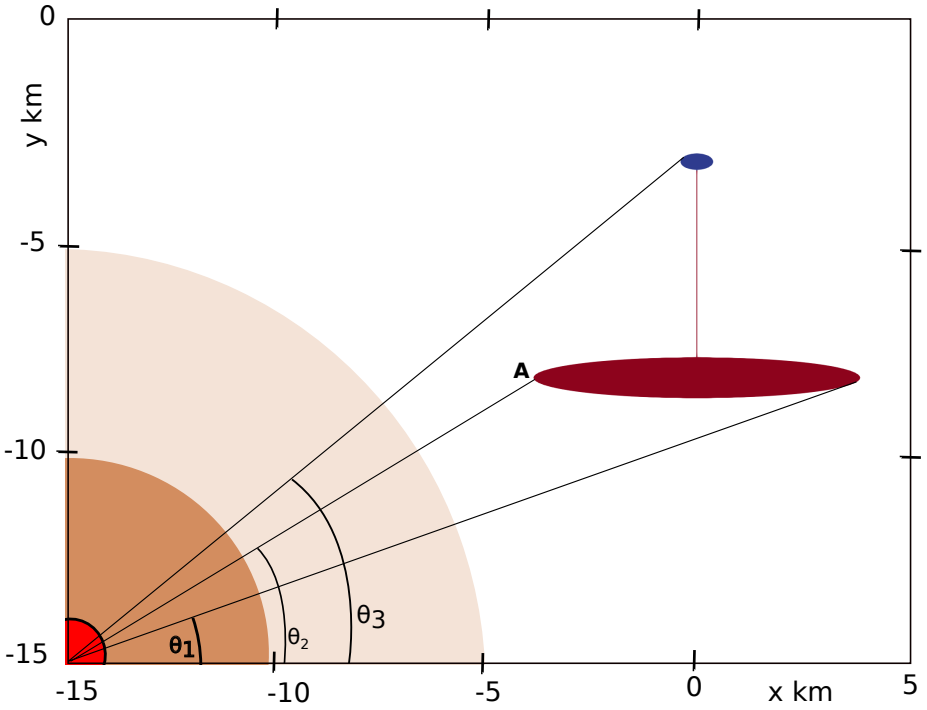

Figure 1: The simulation domain geometry. The epicentre of earthquake is set at 15 km depth and 15 km far from the system axis. The seismic wave strikes the boundary of the system enclosed by θ_1 and θ_3. The objective of this work is to focus on magma dynamics, therefore we do not propagate the wave from the source, instead the wave is assumed to strike at point A at time t = 0 s and for subsequent times the location of strike is computed corresponding to the angle of attack.

shallow chamber is small with respect to the deep one and has an elliptical oblate shape with major and minor axis of length 800 m and 400 m, respectively. The top of the shallow chamber is set at 3000 m below the surface. The two magma chambers are connected through a 20 m wide vertical dike. The thickness of dikes in nature ranges from centimetres to hundreds of metres (Krumbholz et al., 2014). The chosen dike width is representative of feeder dikes observed in active volcanic systems and permits efficient hydraulic communication between the reservoirs. The simulation domain is shown in Figure 1. This simplified geometry approximates many magmatic systems composed of shallow and deep reservoirs (Mangiacapra et al., 2008; Siena et al., 2010; Gudmundsson, 2012)

Magma is modelled as a homogeneous compressible Newtonian mixture. Two magmatic systems are considered: a shoshonite–phonolite (SP) system and an andesite–dacite (AD) system. Each magma is treated as a two-phase homogeneous mixture composed of silicate melt and volatiles. The volatile phase consists of H_2O and CO_2, and the partitioning of volatiles between melt and gas is determined by thermodynamic equilibrium relationships.

For both SP and AD simulations, the deep reservoir and the connecting dike are initially filled with the less evolved volatile-rich magma (shoshonite or andesite), whereas the shallow reservoir contains the more evolved and partially degassed magma (phonolite or dacite). The compositions of the four magmas are reported in Table 1.

In all simulations a straight interface between two magmas is set at the depth of 20 m below the inlet of the shallow chamber, simplifying the condition of arrival of deep magma into the shallow system. The density difference across the interface is 163 kg/m^3 for the SP case, and 215 kg/m^3 for the AD case.

The initial pressure field is obtained by prescribing lithostatic pressure at the roof of the shallow chamber and integrating a magmastatic pressure profile throughout the magmatic system. The initial velocity field is zero everywhere. For simplicity, isothermal conditions are assumed, with temperatures of 1027°C for the SP system and 906°C for the AD system.

3.1 Seismic forcing

In the sets of simulations where we include the passage of a seismic wave, we use the seismic wave data of Petrolia/Cape Mendocino earthquake (Mw 7.2, 1992) (Velasco et al., 1994). The Up and North-South components of the seismic wave are depicted in Figure 2. The objective of this work is to investigate the response of the magmatic system to seismic shaking rather than the propagation of seismic waves through the crust. Therefore, the recorded ground-motion signal is applied directly at the boundary of the magmatic domain instead of modelling wave propagation from the earthquake source through the surround-

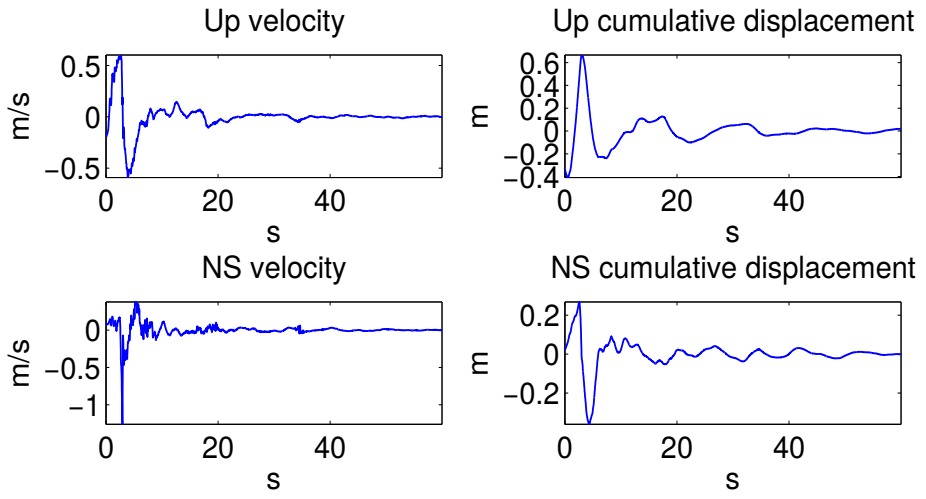

Figure 2: Up and North-South components of the seismic wave.

ing rock. The seismic wave is assumed to shake the magmatic system from the left for first 60 s (Figure 1). To maintain the kinematic equilibrium the velocity on the shaken part of the domain is set equal to the velocity of the seismic wave. On the non-shaken portion of the boundary, the velocity is determined by the elastic mesh-deformation model. For equation (2) the initial deformation is set to zero. On the shaken part of the domain, the displacement of the seismic wave is set as Dirichlet boundary condition and on the non-shaken part of the domain, magma overpressure is assigned as Neumann boundary condition. The computational mesh used in the simulations is composed of 100,000 cells. In order to capture the transient flow features, the mesh is refined near the boundaries. A fixed time step of 0.01 s is used for all simulations, after having verified that such a low time step ensures numerical stability.

4 Results

We first examine the large-scale evolution of magma composition, flow velocity, and overpressure. Particular attention is then devoted to the evolution of overpressure, which exhibits the strongest response to seismic forcing.

4.1 Macroscale mixing

The SP and AD systems mainly differ in magma viscosity, which is approximately 2.9×10^3 Pa·s for the SP case and 3.3×10^4 Pa·s for the AD case. As a consequence, buoyancy-driven convection develops more slowly in the AD simulations (cases 2 and 4), resulting in delayed interface destabilization, plume ascent, and mixing compared with the SP simulations (Table 2).

The simulations indicate that magma viscosity influences the response of the system to seismic shaking. In the lower-viscosity SP case, the buoyant plume exhibits a noticeable lateral deflection during the passage of the seismic wave (case 3), whereas the higher-viscosity AD case shows only minor modifications of the large-scale flow structure.

Despite the limited influence of seismic shaking on large-scale mixing dynamics, its effect on the pressure field is substantial. During and after the first 60 s of shaking, the overpressure distributions in simulations 3 and 4 differ markedly from those obtained in the corresponding non-shaken simulations (Figures 3 and 5). Maximum plume overpressures increase by a factor of approximately six in the SP system and forty in the AD system relative to the corresponding non-shaken simulations (Table 2). In contrast, the compositional evolution and plume ascent remain largely unchanged. For the SP system, the buoyant plume reaches the shallow chamber at approximately the same time in simulations 1 and 3 (Figure 4). Similarly, the AD simulations exhibit only minor differences in plume evolution, with the shaken case showing a delay of less than 30 s relative to the non-shaken case (Figure 6). These observations indicate that seismic forcing primarily modifies the pressure state of the magmatic system while having only a limited impact on the overall convective dynamics.

4.2 Overpressure evolution

We now examine the temporal evolution of overpressure, $\Delta p = p - p_0$, where p_0 is the initial pressure field. The analysis is performed separately for the shallow chamber, dike, and deep chamber. Because overpressure varies spatially throughout the domain, we characterize its evolution using statistical measures computed over all finite elements within each subdomain.

The area-averaged overpressure is defined as

$$\overline{\Delta p} = \frac{\sum_{el=1}^{n} \int_{\Omega_{el}} \Delta p \; d\Omega}{\sum_{el=1}^{n} \int_{\Omega_{el}} 1 \; d\Omega} \tag{5}$$

where Ω_{el} denotes the area of element el and n is the number of elements belonging to the considered subdomain.

Figures 7 and 8 show the temporal evolution of overpressure during the first 300 s. In each panel, the thin dark line represents the area-averaged overpressure $\overline{\Delta p}$, the dark shaded band corresponds to the interquartile range (Q_1–Q_3), and the light shaded region spans the full range between the minimum and maximum values. These statistics provide information on both the average pressure evolution and its spatial variability.

Table 2: Characteristic times, velocities, and overpressures describing the evolution of magma mixing in the shallow chamber.

Overall evolution	Case	Time
Interface destabilization	1,3	20 s
	2,4	80 s
Plume entrance at upper chamber bottom	1,3	60 s
	2,4	180 s
Plume at upper chamber middle	1,3	128 s
	2,4	360 s
Plume velocity at upper chamber middle	1,3	6.0-6.5 m/s
	2,4	3.5 m/s
Plume at upper chamber top	1,3	280 s
	2	520 s
	4	480 s
Plume velocity at upper chamber top (Maximum velocity)	1	8.0 m/s
	2	4.5 m/s
	3	5.0 m/s
	4	3.5 m/s
Plume overpressure at upper chamber top (Maximum overpressure)	1	$2.5 \cdot 10^4$ Pa
	2	$2.0 \cdot 10^4$ Pa
	3	$1.5 \cdot 10^5$ Pa
	4	$8.0 \cdot 10^5$ Pa
Overpressure at 2000 s (shallow chamber)	1	-1.92/-2.83$\cdot 10^5$ Pa (top/bottom)
	2	-1.05/-1.97$\cdot 10^5$ Pa (top/bottom)
	3	-0.86/-1.77$\cdot 10^5$ Pa (top/bottom)
	4	-0.42/-1.40$\cdot 10^5$ Pa (top/bottom)

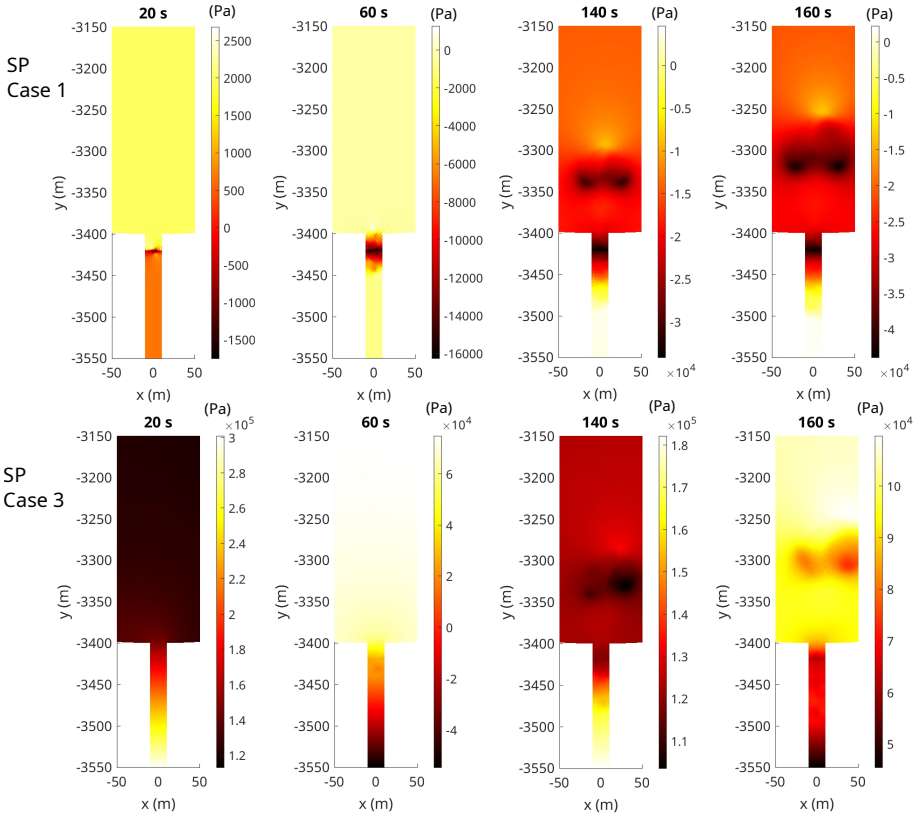

Figure 3: Comparison of overpressure at different time between case 1 and 3.

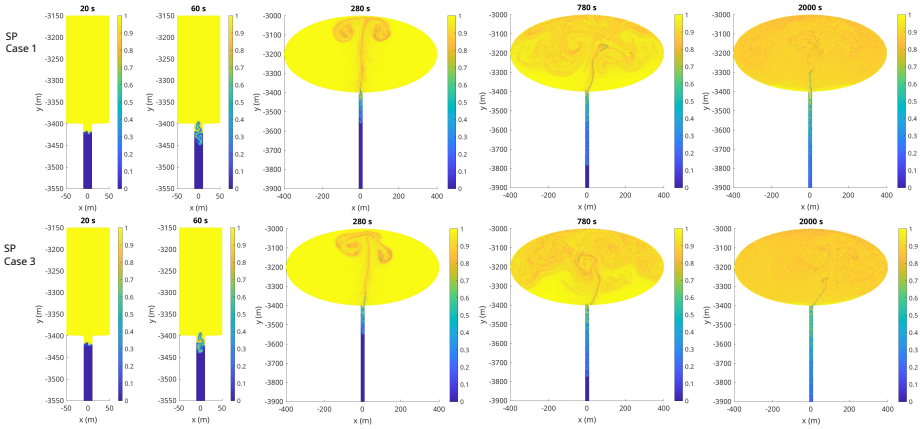

Figure 4: Evolution of composition at different time in case 1 and 3. The composition is represented by the amount of phonolite in the shoshonite-phonolite mixture (0=shoshonite, 1=phonolite). At t = 20 s interface destabilization; t = 60 s entrance of the plume at the shallow chamber bottom; t = 280 s plume at the shallow chamber top; t = 780 s bended secondary plume; t = 2000 s end time of the simulation.

Cases 1 and 2: buoyancy-driven convection without seismic forcing Figure 7 shows the overpressure evolution for the non-shaken simulations. In both cases, buoyancy-driven ascent of low-density magma causes progressive pressure redistribution throughout the magmatic system.

For case 1 (SP system), a small positive overpressure develops during the first few seconds as the density interface destabilizes and buoyant magma begins to rise. Subsequently, the average overpressure in the shallow chamber decreases continuously (Figure 7a). This behaviour reflects the net transfer of magma from the shallow chamber into the dike as the buoyant plume ascends. Localized positive overpressure appears near the chamber roof after approximately 230 s when the rising plume impinges on the upper boundary; however, more than 95% of the chamber volume continues to experience decreasing overpressure.

In contrast, overpressure increases in both the dike and deep chamber (Figures 7b,c). The increase is particularly uniform in the deep chamber, where the spatial variability remains very small. The maximum standard deviations of overpressure are 12.5 kPa, 8.6 kPa, and 58 Pa for the dike, shallow chamber, and deep chamber, respectively (Table 3).

Case 2 exhibits qualitatively similar behaviour (Figures 7d–f), but the evolution occurs over a substantially longer timescale. The higher viscosity of the andesite–dacite system delays interface destabilization and plume ascent, resulting in slower pressure redistribution. Consequently, the decrease of overpressure in the shallow chamber and the increase in the dike and deep chamber occur more gradually than in case 1. The maximum standard deviations remain considerably smaller than those observed in the SP system, reflecting the weaker

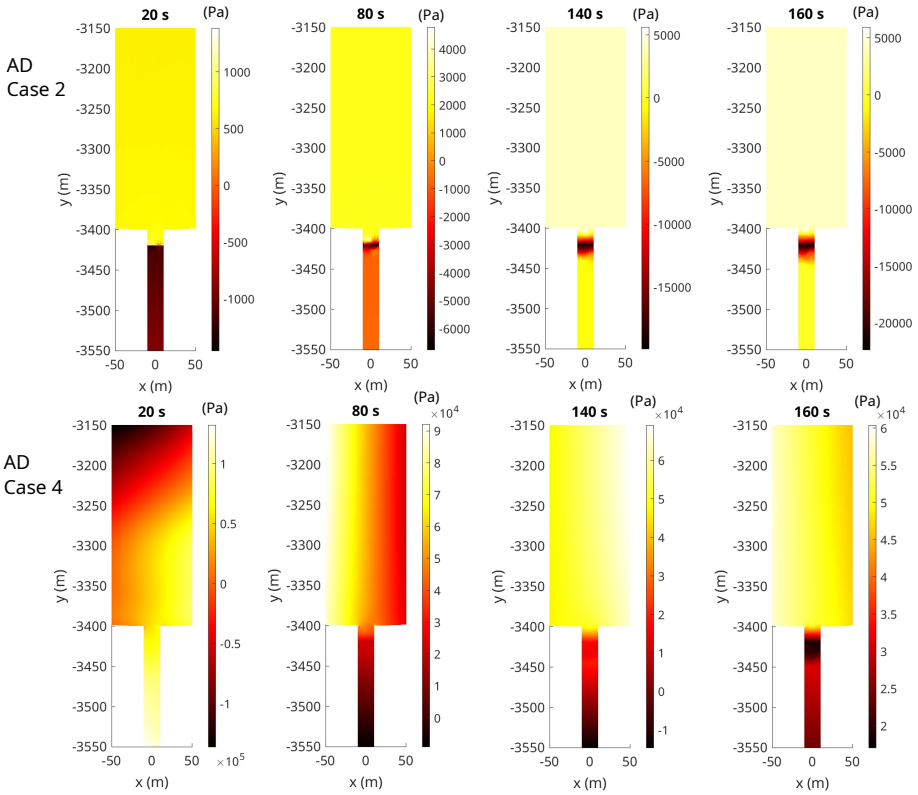

Figure 5: Comparison of overpressure at different time between case 2 and 4.

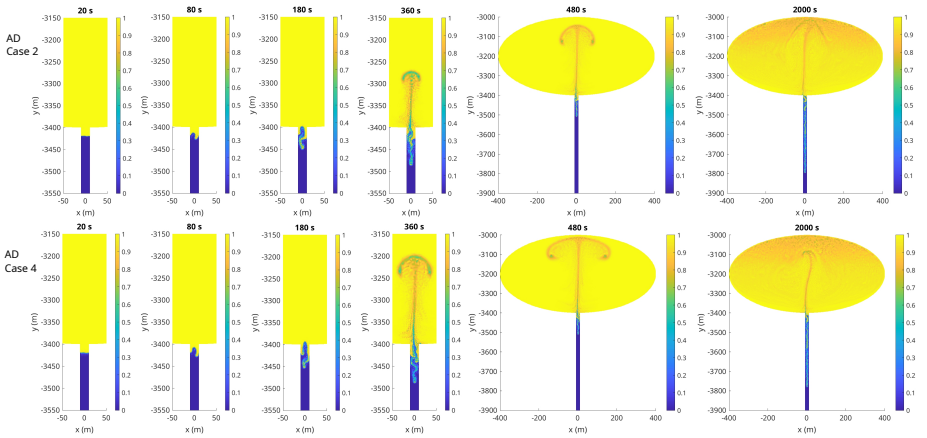

Figure 6: Evolution of composition at different time in case 2 and 4. The composition is represented by the amount of dacite in the andesite-dacite mixture (0=andesite, 1=dacite). At t = 80 s interface destabilization; t = 180 s entrance of the plume at the shallow chamber bottom; t = 360 s plume at the shallow chamber middle; t = 480 s plume at the shallow chamber top; t = 2000 s end time of the simulation.

dynamics associated with the more viscous magma.

Figure 9 compares the long-term evolution of $\overline{\Delta p}$ for cases 1 and 2. The lower-viscosity SP system undergoes more rapid decompression of the shallow chamber and a larger increase of pressure in the deep chamber. In both systems, replacement of volatile-rich magma within the dike by denser magma contributes to pressure increase in the lower parts of the magmatic system.

Cases 3 and 4: convection under seismic shaking The response changes dramatically when seismic shaking is applied. Figure 8 shows that the imposed ground motion generates large-amplitude pressure oscillations throughout the magmatic system.

For case 3 (SP system), overpressure in the shallow chamber varies between approximately −3 and +3 MPa during the first seconds of shaking (Figure 8a). The largest fluctuations occur around 8 s. Similar oscillations are observed in the dike and deep chamber, where overpressure reaches amplitudes exceeding ±5 MPa (Figures 8b,c). The dike exhibits the largest interquartile range, indicating that pressure oscillations are strongest within this narrow conduit. Standard deviations of overpressure reach values of approximately 1.2–1.5 MPa (Table 3), several orders of magnitude larger than in the non-shaken simulations.

Case 4 displays the same overall behaviour but with reduced amplitudes (Figures 8d–f). Maximum overpressure fluctuations in the shallow chamber are limited to approximately ±1.5 MPa, while standard deviations remain below 0.8 MPa. The higher viscosity of the AD system damps pressure oscillations

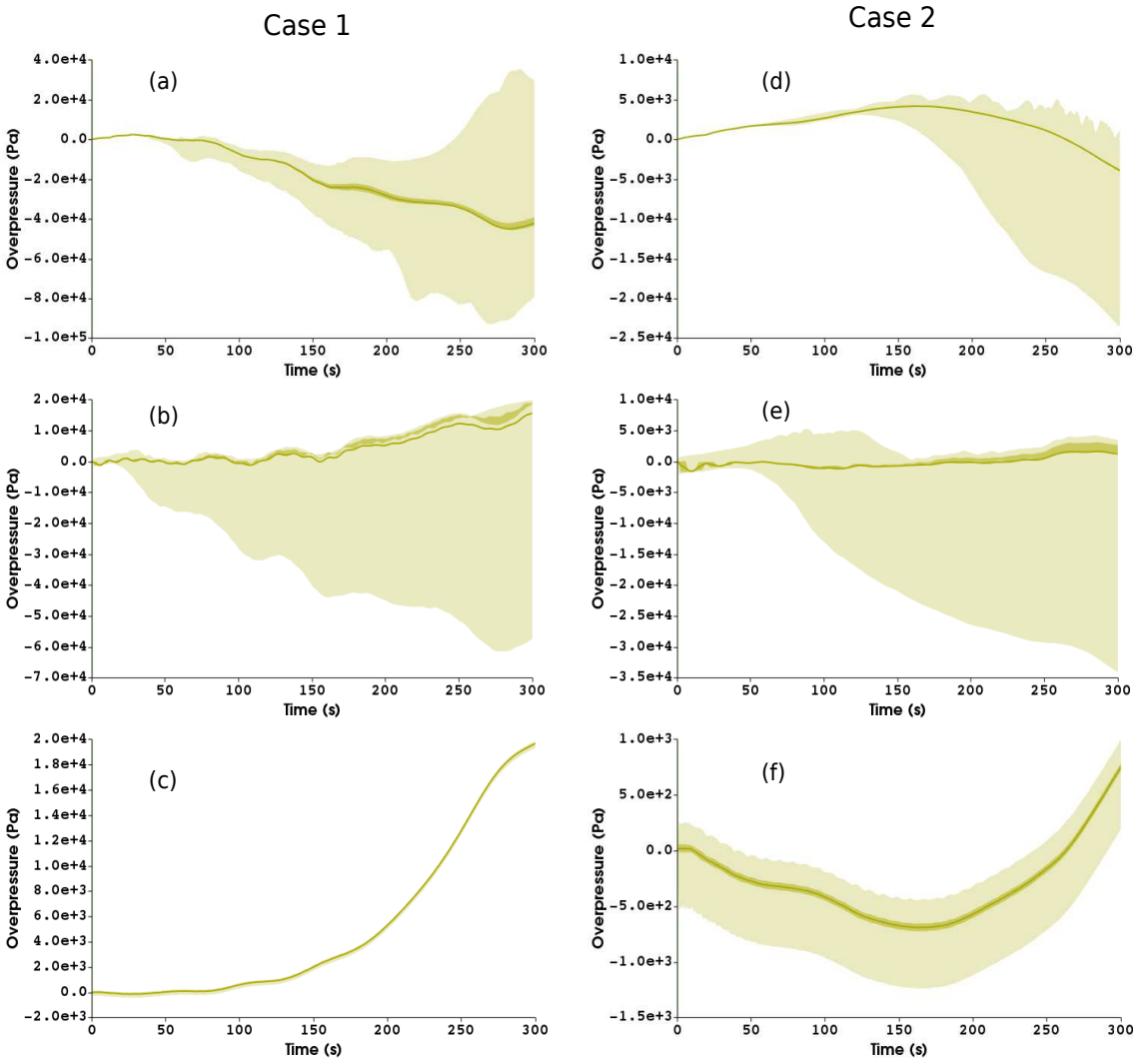

Figure 7: Time series of overpressure for first 300 s. (a), (b) and (c) are for shallow chamber, dike and deep chamber, respectively for case 1. Similarly, (d), (e) and (f) are for shallow chamber, dike and deep chamber, respectively, for case 2.

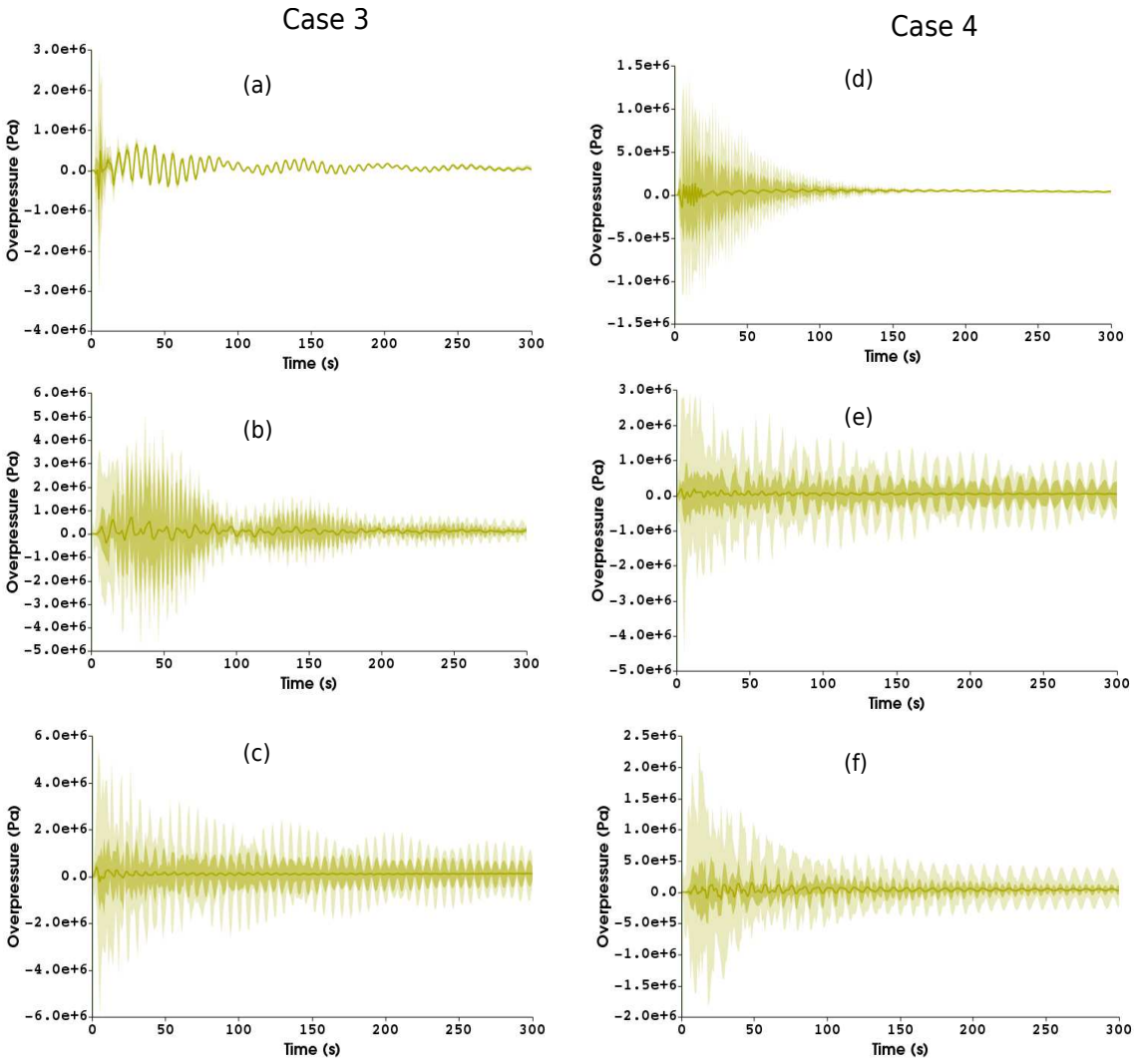

Figure 8: Time series of overpressure for first 300 s. (a), (b) and (c) are for the shallow chamber, dike and deep chamber, respectively for case 3. Similarly, (d), (e) and (f) are for shallow chamber, dike and deep chamber, respectively for case 4.

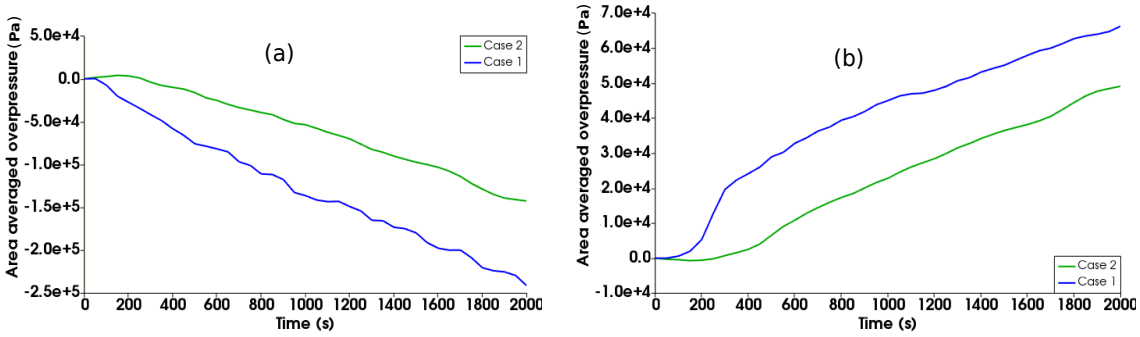

Figure 9: Time series of area averaged overpressure ($\overline{\Delta p}$) up to 2000 s for simulation case 1 and 2. (a) shallow chamber, (b) deep chamber

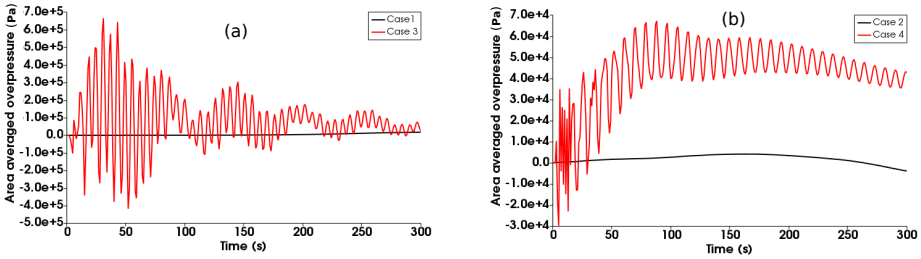

Figure 10: Comparison of area averaged overpressure ($\overline{\Delta p}$) in shallow chamber for first 300 s between simulation case 1,3 and 2,4

and suppresses secondary resonant behaviour that is clearly visible in case 3.

The oscillatory pressure signal is approximately symmetric around zero mean pressure, indicating that compression and decompression phases contribute nearly equally to the pressure response. The observed oscillations result from repeated reflection of pressure waves within the magmatic system and their interaction with chamber boundaries.

Comparison of shaken and non-shaken simulations Figure 10 directly compares the evolution of $\overline{\Delta p}$ in the shallow chamber for all four simulations. In the absence of seismic forcing (cases 1 and 2), overpressure evolves smoothly as a consequence of buoyancy-driven magma transport. In contrast, seismic shaking generates oscillatory pressure signals whose amplitudes exceed those produced by convection alone by several orders of magnitude.

Although seismic shaking substantially modifies the pressure field, its influence on magma transport remains comparatively limited. As discussed in the previous section, the timing of plume ascent and compositional evolution differs only slightly between shaken and non-shaken simulations. The dominant effect of seismic forcing is therefore the generation of transient overpressure waves

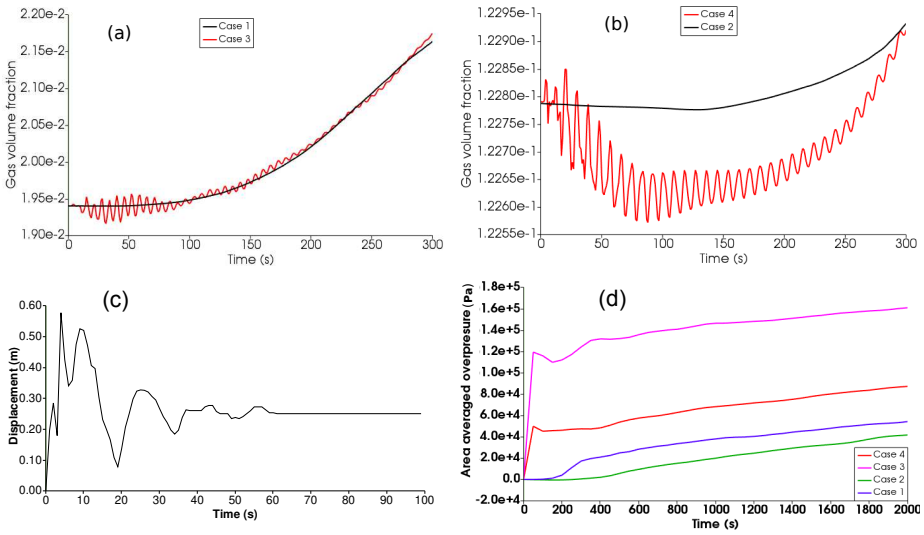

Figure 11: Comparison of global diagnostics for the four simulations. (a) and (b) Averaged gas volume fraction in the shallow chamber during the first 300 s. (c) Displacement of an arbitrarily selected node on the non-shaken boundary of the lower chamber during the first 100 s. (d) Domain-averaged overpressure ($\overline{\Delta p}$) during the 2000 s simulation period. Cases 1 and 2 correspond to simulations without seismic shaking, whereas Cases 3 and 4 include seismic shaking.

rather than a major alteration of convective flow dynamics.

Long-term evolution Figure 11 shows the average gas volume fraction within the shallow chamber. Despite the large transient pressure fluctuations observed during seismic shaking, no substantial changes in gas content are detected during the first 300 s.

The imposed seismic motion also generates deformation of the computational domain. Figure 11c shows the displacement of a representative node located on the non-shaken boundary of the deep chamber. Maximum displacement reaches approximately 0.58 m after 6 s and subsequently decays as the seismic excitation diminishes.

The long-term evolution of the domain-averaged pressure perturbation also differs substantially between shaken and non-shaken simulations. After 2000 s, $\overline{\Delta p}$ in case 4 remains approximately three times larger than in case 2, whereas case 3 exhibits values nearly one order of magnitude larger than case 1 (Figure 11d). These results indicate that a short-lived seismic perturbation can influence the long-term pressure evolution of a magmatic system well beyond the duration of the imposed shaking.

Table 3: The results of numerical simulations for first 300 s. The values below 1 kPa are not reported in the interquartile range.

Case	Domain	Δp (MPa)	Q_1-Q_3 (MPa)	σ (MPa)
1	Shallow chamber	(-0.094) - 0.039	(-0.047) - 0.002	0.862×10^{-2}
	Dike	(-0.061) - 0.020	(-0.001) - 0.001	0.124×10^{-1}
	Deep chamber	(-0.001) - 0.019	-	0.583×10^{-4}
2	Shallow chamber	(-0.023) - 0.006	(-0.003) - 0.001	0.878×10^{-3}
	Dike	(-0.034) - 0.005	(-0.001) - 0.001	0.448×10^{-2}
	Deep chamber	(-0.001) - 0.001	-	0.701×10^{-4}
3	Shallow chamber	(-3.066) - 2.894	(-1.747) - 1.337	1.379
	Dike	(-4.554) - 5.074	(-2.559) - 3.058	1.158
	Deep chamber	(-5.038) - 5.195	(-1.537) - 1.587	1.539
4	Shallow chamber	(-1.234) - 1.467	(-0.699) - 0.847	0.789
	Dike	(-4.436) - 2.946	(-0.846) - 0.958	0.636
	Deep chamber	(-1.846) - 2.378	(-0.582) - 0.580	0.681

5 Discussion

In this work we investigated how transient seismic shaking modifies the evolution of a buoyancy-driven magmatic system composed of compositionally distinct magmas. The simulations were designed to isolate the effects of seismic forcing by comparing otherwise identical scenarios with and without earthquake-induced shaking. Initially, the two magmas are separated by a sharp compositional interface, representing the onset of magma interaction following the arrival of deeper, less evolved magma into a shallow reservoir. The simulations were performed in 2D as the previous studies demonstrated that the large-scale evolution of buoyancy-driven magma mixing is captured satisfactorily in two dimensions while reducing computational cost (Garg and Papale, 2022).

The simulations demonstrate that magma viscosity exerts a first-order control on the rate of convective mixing. The lower-viscosity SP system develops buoyant instabilities rapidly, leading to efficient mixing within the simulation time, whereas the higher-viscosity AD system evolves more slowly and remains only partially mixed after 2000 s. This behaviour is consistent with previous studies showing that increasing magma viscosity suppresses interface deformation, plume ascent and mixing efficiency (Couch et al., 2001).

The simulations indicate that decompression within the shallow chamber is accompanied by compression within the dike and deep reservoir. The net increase in domain-averaged overpressure suggests that pressure redistribution within the plumbing system is not spatially balanced and may contribute to ground uplift. In some cases the ground deformation can be accredited to the deep magma source. At Karymsky volcano a widespread extension was measured during the period 1983–1994 (Maguskin et al., 1993). The bulk of mea-

sured surface deformation was attributed to the inflation of a large deep magma reservoir situated at 18 km depth (Fedotov, 1998). The results highlight the importance of considering the entire magmatic system when interpreting pressure evolution and associated geophysical signals rather than focusing solely on shallow reservoirs.

In cases 1 and 2 overpressure varies smoothly in all parts of the domain, whereas, in cases 3 and 4 we see that shaking of the domain generates an overpressure wave in the system. The overpressure fluctuations show an instantaneous compression and extension. However, looking at the macro scale magma mixing, no major changes were observed. Particularly, the effect of shaking on magma transport, plume ascent and the composition evolution remains limited. Seismic shaking generates transient overpressure oscillations with amplitudes reaching several megapascals, whereas the corresponding effects on magma transport and compositional evolution remain limited. The strongest response is observed in the lower-viscosity SP system, indicating that low-viscosity magmas transmit and sustain pressure disturbances more efficiently than high-viscosity magmas. Although the seismic overpressure waves decay through viscous damping, the simulations show that the pressure field does not immediately return to the state obtained in the non-shaken cases. The transient pressure oscillations generated during shaking modify the early evolution of the magmatic system, resulting in a different redistribution of pressure. Consequently, persistent differences in overpressure remain long after the cessation of seismic forcing.

The largest pressure oscillations occur within the dike, where peak overpressures approach 5 MPa. These values are comparable to reported tensile strengths of volcanic host rocks (Gudmundsson, 2016). Although the present model does not include rock failure or fracture propagation, the results suggest that transient earthquake-induced pressure fluctuations may locally modify the mechanical state of dike walls and potentially contribute to fracture reactivation under favourable conditions. Moreover, in our simulations the impinging was done at the beginning of the simulation when the mingling between the two magmas was not started. We observed in cases 1 and 2 that in case of dominating buoyancy forces the deep system may have a compression which progressively increases with time. If the earthquake strikes at a time when the system is already under the evolution i.e. the magma at the depth is already experiencing a compression, which is most likely to exist in a real volcanic system, the rise in Δp may be higher. Further work is clearly needed to model a scenario in which earthquake strikes when mixing is already ongoing. In a case when the overpressure is close to its critical value i.e. it is approaching to the tensile strength of the wall, such transient pressure increases may contribute to reaching failure conditions in systems that are already close to critical overpressure.

In Linde et al. (1994) the authors proposed that the gas bubbles may be shaken loose and rise within magma during the passage of a seismic wave. In

our results apart from the high fluctuations of Δp, we did not find any substantial changes in the amount of exsolved volatiles. One possible reason for this can be that in our numerical simulations the domain was fully filled with magmas without leaving an extra space. Therefore, the magma did not have sufficient free surface to undergo significant sloshing and to increase the mobility of the volatiles in the melt. In Namiki et al. (2016) authors performed several shaking simulations with analogue materials having a similar viscosity of basalt to investigate how sloshing can affect a volcanic system. They concluded that the sloshing is mainly effective for a partially filled tank which can collapse the foam gathered at the top of the tank and can increase the gas content. The numerical simulations carried out in this work are without a foam layer at the top, in such a case the only possibility of an increment of gas is the reduction of the solubility of volatiles in the magma. For a constant temperature the solubility of volatiles inside a magma largely depends on the pressure. The rapid pressure oscillations generated by the seismic wave produce only transient variations in volatile solubility and gas volume fraction, resulting in negligible net changes in exsolved gas content over the simulated timescale.

In this work our aim was to focus on magma dynamics, therefore, we did not account the stress changes in the surrounding rock which can be an additional factor in affecting the magmatic system as well as triggering an eruption (Walter and Amelung, 2007; Diez et al., 2005; Wang et al., 2011). Earthquakes can modify the stress field around a magmatic system and in the proximity of the volcano either in a static or in a dynamic way (Manga and Brodsky, 2006; Walter and Amelung, 2007; Watt et al., 2009). Static stress change decays as the inverse cube of the distance from the hypocenter and therefore considered to be effective only within the near field (Bebbington and Marzocchi, 2011; Hill and Prejean, 2007). Dynamic stress changes are generated by the seismic waves and can propagate over much greater distances (Walter and Amelung, 2007). A decrease in stress in the volcanic edifice can enhance the exsolution of dissolved gases and can contribute to magma compression. On the other hand, an increased stress in the volcanic edifice may cause a volumetric contraction and an increase in overpressure. A complete analysis of the problem requires a two-way coupling between magma and the surrounding rock which was not in the scope of the current work. Previous studies (Manga and Brodsky, 2006; Hong et al., 2016)indicate that earthquake-induced stress changes in the surrounding rock are commonly of the order of hundreds of kilopascals, whereas the pressure fluctuations predicted here reach several megapascals. Although direct comparison is difficult because the present study neglects magma-rock coupling, these results suggest that fluid overpressure generated within the magmatic system may constitute an important component of the overall response to seismic forcing. Magma overpressure is widely regarded as one of the principal controls on dike propagation and eruption initiation. Nevertheless, looking at only magma dynamics gives us a clear idea that even in an end member case where there are only buoyancy forces acting in the system, overpressure largely varies during and after an earthquake, which ultimately determines the fate of the magma

plumbing system.

Overall, the simulations indicate that seismic shaking primarily influences the pressure evolution of a magmatic system rather than its large-scale mixing dynamics. While the imposed earthquake does not substantially modify plume ascent or compositional transport, it generates pressure oscillations of several megapascals and leaves a persistent overpressure signature after the shaking has ceased. These findings support the hypothesis that earthquakes may influence volcanic systems by perturbing their internal pressure state, thereby modifying the conditions that control dike propagation and eruption triggering.

6 Summary and conclusions

We performed numerical simulations to investigate the response of a magmatic plumbing system to transient seismic shaking. The model consists of a deep reservoir, a shallow reservoir, and a connecting dike, and considers magma mixing driven by buoyancy forces in both shaken and non-shaken conditions. Two representative magma systems were analysed: a low-viscosity shoshonite–phonolite (SP) system and a higher-viscosity andesite–dacite (AD) system.

The simulations show that magma viscosity exerts a first-order control on mixing dynamics, with the SP system exhibiting faster plume development and more efficient mixing than the AD system. In contrast, the influence of seismic shaking on large-scale magma transport is limited. The timing of interface destabilization, plume ascent, and compositional evolution remains largely unchanged between shaken and non-shaken simulations.

The most significant effect of seismic shaking is observed in the pressure field. The passage of the seismic wave generates transient overpressure oscillations throughout the magmatic system, with the largest amplitudes occurring within the dike. In the SP simulations, overpressure fluctuates between approximately -3 and $+3$ MPa in the shallow chamber and reaches amplitudes exceeding 5 MPa in the dike and deep reservoir. In the AD simulations, pressure oscillations reach approximately 2–4 MPa depending on the location within the system. These transient pressure disturbances exceed the overpressure variations associated with buoyancy-driven convection by one to two orders of magnitude.

Although the seismic overpressure waves are progressively damped by magma viscosity, the pressure field does not immediately return to the state obtained in the non-shaken simulations. Instead, elevated overpressure levels persist long after the cessation of seismic forcing, indicating that transient seismic perturbations can produce lasting modifications of the pressure state of a magmatic system.

Overall, the results suggest that earthquakes may influence volcanic systems primarily through pressure perturbations rather than through direct modification of magma mixing dynamics. While the present study does not include magma-rock mechanical coupling or fracture propagation, the predicted pressure oscillations reach magnitudes comparable to reported tensile strengths of

volcanic rocks, indicating that seismic shaking may contribute to conditions favourable for dike reactivation and eruption triggering in magmatic systems that are already close to critical failure conditions.

Declarations

Funding No funding was received for conducting this study.

Ethics approval and consent to participate Not applicable.

Data availability The software, GALES, used to do simulations is open source and is available at https://gitlab.com/dgmaths9/gales. The simulations data presented in the article can be requested to the authors by contacting the corresponding author.

Author contributions D.G. conceived and performed the numerical simulations, developed the computational methodology, analysed the results, prepared the figures, and wrote the original manuscript draft. A.L. contributed to the interpretation of the results, volcanological analysis, and manuscript revision. P.P. contributed to the study conception, scientific supervision, interpretation of the results, and manuscript revision. All authors reviewed and approved the final manuscript.

Competing interests The authors declare no competing interests.

References

M. Alam and M. Kimura. Statistical analysis of time-distance relationship between volcanic eruptions and great earthquakes in japan. Earth Planets and Space, 56:179–192, 2004.

M.S. Bebbington and W. Marzocchi. Stochastic models for earthquake triggering of volcanic eruptions. Journal of Geophysical Research, 116:1–16, 2011.

F.L. Bonali et al. Quantifying the effect of large earthquakes in promoting eruptions due to stress changes on magma pathway: The chile case. Tectonophysics, 583:54–67, 2012.

C.W. Burnham et al. Thermodynamic properties of water to 1,000°c and 10,000 bars. Geological Society of America Special Papers, 132:1–96, 1969.

S. Couch et al. Mineral disequilibrium in lavas explained by convective self-mixing in open magma chambers. Nature, 411:1037–1039, 2001.

J.B. Crews and C.A. Cooper. Experimental evidence for seismically initiated gas bubble nucleation and growth in groundwater as a mechanism for coseismic borehole water level rise and remotely triggered seismicity. Journal of Geophysical Research B: Solid Earth, 119:1–13, 2014.

M. Diez et al. Evidence for static stress changes triggering the 1999 eruption of cerro negro volcano, nicaragua and regional aftershock sequences. Geophys. Res. Lett., 32(L04309):1–4, 2005.

S. Eggert and T.R. Walter. Volcanic activity before and after large tectonic earthquakes: Observations and statistical significance. Tectonophysics, 471: 14–26, 2009.

S.A. Fedotov. Study and mechanism of simultaneous 1996 karymsky volcano and akademii nauk caldera eruptions in kamchatka. volcanology and seismology, 19:525–566, 1998.

E. Fujita et al. Stress field change around the mount fuji volcano magma system caused by the tohoku megathrust earthquake. Japan. Bull. Volcanol., 75:679, 2013.

D. Garg. A finite element method for magma-rock interaction dynamics in volcanic environment. PhD thesis, University of Florence, 2017.

Deepak Garg and Paolo Papale. High-performance computing of 3d magma dynamics, and comparison with 2d simulation results. Frontiers in Earth Science, Volume 9 - 2021, 2022. doi: 10.3389/feart.2021.760773. URL `https://www.frontiersin.org/journals/earth-science/articles/10.3389/feart.2021.760773`.

Deepak Garg, Antonella Longo, and Paolo Papale. Computation of compressible and incompressible flows with a space–time stabilized finite element method. Computers & Mathematics with Applications, 75(12):4272–4285, 2018a. ISSN 0898-1221. doi: https://doi.org/10.1016/j.camwa.2018.03.028.

Deepak Garg, Antonella Longo, and Paolo Papale. Modeling free surface flows using stabilized finite element method. Mathematical Problems in Engineering, 2018(1):6154251, 2018b. doi: https://doi.org/10.1155/2018/6154251. URL `https://onlinelibrary.wiley.com/doi/abs/10.1155/2018/6154251`.

Deepak Garg, Paolo Papale, and Antonella Longo. A partitioned solver for compressible/incompressible fluid flow and light structure. Comput. Math. Appl., 100(C):182–195, 2021. ISSN 0898-1221. doi: 10.1016/j.camwa.2021.09.005.

D. Giordano et al. Viscosity of magmatic liquids: a model. Earth and Planetary Science Letters, 271:123–134, 2008.

A. Gudmundsson. The mechanics of large volcanic eruptions. Earth-Science Reviews, 163:72–93, 2016.

Agust Gudmundsson. Magma chambers: Formation, local stresses, excess pressures, and compartments. Journal of Volcanology and Geothermal Research, 237-238:19–41, 2012.

D.P. Hill and S.G. Prejean. Dynamic triggering. Treatise Geophys, 4:257–291, 2007.

D.P. Hill et al. Earthquake-volcano interactions. Phys. Today, 55:41–47, 2002.

T.K. Hong et al. Prediction of ground motion and dynamic stress change in baekdusan (changbaishan) volcano caused by a north korean nuclear explosion. Scientific reports, 6(21477):1–8, 2016.

M. Ichihara and E. Brodsky. A limit on the effect of rectified diffusion in volcanic systems. Geophysical Research Letters, 33:1–5, 2006.

M. Ishii and N. Zuber. Drag coefficient and relative velocity in bubbly, dropletor particulate flows. AiChE Journal, 25:843–855, 1979.

R.C. Jachens and G.P. Eaton. Geophysical observations of kilauea volcano, hawaii, 1. temporal gravity variations related to the 29 november, 1975, m = 7.2 earthquake and associated summit collapse. Journal of Volcanology and Geothermal Research, 7:225–240, 1980.

Philippe Jousset, Jürgen Neuberg, and Arthur Jolly. Modelling low-frequency volcanic earthquakes in a viscoelastic medium with topography. Geophysical Journal International, 159(2):776–802, 2004. doi: https://doi.org/10.1111/j.1365-246X.2004.02411.x.

Michael Krumbholz, Christoph F. Hieronymus, Steffi Burchardt, Valentin R. Troll, David C. Tanner, and Nadine Friese. Weibull-distributed dyke thickness reflects probabilistic character of host-rock strength. Nature Communications, 5:3272, 2014. doi: 10.1038/ncomms4272. URL `https://doi.org/10.1038/ncomms4272`.

R.A. Lange. The effects of H_2O, CO_2 and F on the density and viscosity of silicate melts. Reviews of Mineralogy, 30:331–369, 1994.

L.E. Lara et al. Rhyodacitic fissure eruption in southern andes (cordón caulle; 40.5°s) after the 1960 (mw:9.5) chilean earthquake: a structural interpretation. Journal of Volcanology and Geothermal Research, 138:127–138, 2004.

T. Lay et al. Teleseismic inversion for rupture process of the 27 february 2010 chile (mw 8.8) earthquake. Geophysical Research Letters, 37(L13301):1–5, 2010.

Fabian Limberger and Georg Rümpker. Numerical modeling predicts seismic resonances in the magma chamber-conduit system due to wavefield capturing. Volcanica, 7:461–470, 07 2024. doi: 10.30909/vol.07.02.461470.

A.T. Linde and I.S. Sacks. Triggering of volcanic eruptions. Nature, 395:888–890, 1998.

A.T. Linde et al. Increased pressure from rising bubbles as a mechanism for remotely triggered seismicity. Nature, 371:408–410, 1994.

A. Longo, D. Garg, P. Papale, and C. P. Montagna. Dynamics of magma chamber replenishment under buoyancy and pressure forces. Journal of Geophysical Research: Solid Earth, 128(1):e2022JB025316, 2023. doi: https://doi.org/10.1029/2022JB025316.

A. Longo et al. A finite element galerkin/least-squares method for computation of multicomponent compressible-incompressible flows. Computers and Fluids, 67:57–71, 2012.

M.A. Maguskin et al. Ground surface deformation in karymskiy volcanic area. volcanology and seismology, 14:450–470, 1993.

M. Manga and E.E. Brodsky. Seismic triggering of eruptions in the far field: volcanoes and geysers. Annual Review of Earth and Planetary Sciences, 34: 263–291, 2006.

M. Manga et al. Earthquake triggering of mud volcanoes. Marine and Petroleum Geology, 26:1785–1798, 2009.

A. Mangiacapra et al. The deep magmatic system of the campi flegrei caldera (italy). Geophys Res Lett, 35(L21304):1–6, 2008.

W. Marzocchi. Remote seismic influence on large explosive eruptions. Geophysical Research, 107:1–7, 2002.

W. Marzocchi et al. Modeling the stress variations induced by great earthquakes on the largest volcanic eruptions of the 20th century. Journal of Geophysical Research B: Solid Earth, 107(ESE 13):1–8, 2002.

A. Namiki et al. Sloshing of a bubbly magma reservoir as a mechanism of triggered eruptions. Journal of Volcanology and Geothermal Research, 320: 156–171, 2016.

T. Nishimura. Triggering of volcanic eruptions by large earthquakes. Geophysical research letters, 44:7750–7756, 2017.

P. Papale et al. The compositional dependence of the multicomponent volatile saturation surface in silicate melts. Chem Geol, 229:78–95, 2006.

M.E. Pritchard et al. Subsidence at southern andes volcanoes induced by the 2010 maule, chile earthquake. Nature Geoscience, 6:632–636, 2013.

L. De Siena et al. Seismic attenuation imaging of campi flegrei caldera: architecture and temporal evolution. Journal of Geophysical Research, 115:1–18, 2010.

K. Stein, T. Tezduyar, and R. Benney. Mesh moving techniques for fluid-structure interactions with large displacements. Journal of Applied Mechanics, 70:58–63, 2003.

Susan Sturton and Jürgen Neuberg. The effects of a decompression on seismic parameter profiles in a gas-charged magma. Journal of Volcanology and Geothermal Research, 128(1):187–199, 2003. ISSN 0377-0273. doi: https://doi.org/10.1016/S0377-0273(03)00254-3. Putting Volcano Seismology in a Physical Context. In memory of Bruno Martinelli.

Y. Takada and Y. Fukushima. Volcanic subsidence triggered by the 2011 tohoku earthquake in japan. Nat. Geosci, 6:637–631, 2013.

T.E. Tezduyar. Computation of moving boundaries and interfaces and stabilization parameters. I.J. for Numerical Methods in Fluids, 43:555–575, 2003.

W. Thatcher and J.C. Savage. Triggering of large earthquakes by magma-chamber inflation, izu peninsula. Japan, Geology (Boulder), 10:637–640, 1982.

S. Toda et al. Widespread seismicity excitation throughout central japan following the 2011 m=9.0 tohoku earthquake and its interpretation by coulomb stress transfer. Geophysical Research Letters, 38(L00G03):1–5, 2011.

A.A. Velasco et al. Recent large earthquakes near cape mendocino and in the gorda plate: Broadband source time functions, fault orientations, and rupture complexities. Journal of Geophysical Research, 99:711–728, 1994.

T.R. Walter and F. Amelung. Volcano-earthquake interaction at mauna loa volcano, hawaii. Journal of Geophyiscal Research, 111(B05204):1–17, 2006.

T.R. Walter and F. Amelung. Volcanic eruptions following m $\geq$ 9 megathrust earthquakes: Implications for the sumatra-andaman volcanoes. Geology, 35: 539–542, 2007.

F. Wang et al. Influence of the march 11, 2011 mw 9.0 tohoku-oki earthquake on regional volcanic activities. Chinese Sci. Bull., 56:2077–2081, 2011.

S.F.L. Watt et al. The influence of great earthquakes on volcanic eruption rate along the chilean subduction zone. Earth and Planetary Science Letters, 277: 399–407, 2009.

L. Zong et al. Ground deformation associated with the march 1996 earthquake swarm at akutan volcano, alaska, revealed by satellite radar interferometry. JOURNAL OF GEOPHYSICAL RESEARCH, 105(B9):21483–21495, 2000.

Óscar E. Cadena and John J. Sánchez. Conduit resonance models for long-period seismicity at galeras volcano (colombia), during 2004–2010. Journal of South American Earth Sciences, 113:103661, 2022. ISSN 0895-9811. doi: https://doi.org/10.1016/j.jsames.2021.103661.